A General Approach for Direct Wet Transfer of Large-Area Optoelectronic Hybrid Perovskite Single-Crystalline Thin-Films

*Ran Ding, Chun-Ki Liu, Zehan Wu, Feng Guo, Sin-Yi Pang, Lok Wing Wong, Weng Fu Io, Shuoguo Yuan, Man-Chung Wong, Michal Bartlomiej Jedrzejczyk, Jiong Zhao, Feng Yan and Jianhua Hao**

Dr. R. Ding, C. -K. Liu, Z. Wu, F. Guo, S. -Y. Pang, W. F. Io, S. Yuan. Dr. M. -C. Wong, M. B. Jedrzejczyk, Dr. J. Zhao, Prof. F. Yan, Prof. J. Hao, Department of Applied Physics, The Hong Kong Polytechnic University, Hung Hom, Hong Kong, China.
E-mail: jh.hao@polyu.edu.hk

Keywords: (perovskite single-crystalline films, wet transfer method, $FAPbBr_3$, photodetectors)

Hybrid perovskite single-crystalline films are promising for making high-performance perovskite optoelectronic devices due to their superior physical properties compared to the polycrystalline counterpart. However, the key issue in using the films is that it is challenging to incorporate them into multilayer devices because of their on-substrate growth. Here, a wet transfer method is used in transferring perovskite single-crystalline films perfectly onto various target substrates for the first time. More importantly, we show that the large millimeter-scaled single-crystalline films as thin as a few hundred nanometers are capable of sustaining their excellent crystalline quality and morphology after the transferring process. The availability of the unique large-area and single-crystalline perovskite thin-films offers us a convenient route to further investigate the optical and optoelectronic properties of hybrid perovskites. The use of this method in fabricating perovskite single-crystalline film-based photodetectors is further demonstrated with a remarkable photoresponsivity. It is expectable that this transferring strategy would support broad applications of perovskite single-crystalline films for more complex multilayer perovskite devices.

Ding, R., Liu, C. K., Wu, Z., Guo, F., Pang, S. Y., Wong, L. W., ... & Hao, J. (2020). A general wet transferring approach for diffusion-facilitated space-confined grown perovskite single-crystalline optoelectronic thin films. Nano Letters, 20(4), 2747-2755.

Over the past few years, hybrid organic-inorganic halide perovskites have made great progress in the field of optoelectronic devices due to their numerous advantageous properties, such as high absorption coefficient, tunable bandgap, and long-ranged balanced electron and hole transport.[1-16] The power conversion of perovskite solar cells has reached a milestone of 25.2% in single-junction architectures since the first report in 2009, emerging as a competitive contender for traditional silicon solar cells.[17] Due to the facile solution processability, the perovskite films employed in devices so far are typically polycrystalline, containing many small voids, grain boundaries and surface imperfections.[18-20] A number of previous studies have shown a high trap state density existed within the perovskite polycrystalline films which cause an obstruction of the ultimate performance of perovskite devices.[21,22] Therefore, the strategy of growing perovskite single-crystalline films provides a potential solution to overcome this obstacle.

Recently, Wan *et al.* reported a spatial confinement method to obtain perovskite single-crystalline films by clipping two substrates together to dip into perovskite precursor solution. The method enabled an on-substrate growth of various perovskite single-crystalline films in a size of submillimeter with adjustable thicknesses from nano- to micrometers.[23] Later, photodetectors based on $CH_3NH_3PbBr_3$ ($MAPbBr_3$) single-crystalline films were fabricated by following this method which exhibited a record photoconductive gain of 50 million and a gain-bandwidth product of 70 GHz.[24] Huang *et al.* improved this method by adding a hydrophobic layer to accelerate ion diffusion which also acted as a hole transport material in perovskite solar cells.[25] A power conversion of 17.8% was achieved by optimizing the below-bandgap absorption of $MAPbI_3$ single-crystalline films. Also, field-effect transistors were tried with different $MAPbX_3$ (X = Cl, Br, I) single-crystalline films, yielding record room-temperature field-effect behaviors.[26] Thus, perovskite single-crystalline films seem to be a promising candidate for enhancing perovskite photoelectric device performance due to their superior physical properties compared to the polycrystalline counterpart.

However, the study of perovskite single-crystalline films still meets with some problems for further practical applications. The major obstacle in using these films is their on-substrate growth which makes it difficult to integrate with other functional semiconducting and metallic layers for hybrid multilayer optoelectronic devices. After crystallization growth, the perovskite single-crystalline films are normally fixed on the given substrate with strong adhesion.[23-26] Transferring perovskite single-crystalline films is found out to be technically challenging owing to the water-sensitivity of perovskite materials which are incompatible with conventional transfer methods.[27,28] This limitation will impede the use of perovskite single-crystalline films for more complex multilayer perovskite devices. To this end, a rational transferring strategy to perfectly transfer perovskite single-crystalline films onto other functional materials will allow scalable fabrication of high-performance perovskite devices.

In this work, millimeter-sized perovskite single-crystalline films can be grown with controlled thickness down to around 100 nm by a diffusion-facilitated spatial confinement method. Relying on the introduction of a hydrophobic layer on substrates, perovskite single-crystalline films can be easily peeled off and transferred onto arbitrary target substrates based on a facile wet transfer method. Further studies reveal that the perovskite single-crystalline films sustain high crystalline quality and morphology after the transferring process. On this basis, we show this method can be used as a general approach to transfer different kinds of perovskite single-crystalline films, including $FAPbBr_3$, $MAPbI_3$ and $CsPbBr_3$. The availability of the unique large-area and single-crystalline perovskite thin-films opens up opportunities for study on the optical and optoelectronic properties of hybrid perovskites. Later, the $FAPbBr_3$ single-crystalline films are obtained and directly transferred onto patterned interdigital Au electrodes for the fabrication of photodetectors, which exhibit a comparable photoresponsivity to that of the state-of-the-art perovskite single-crystalline film-based photodetectors. These results demonstrate that this wet transfer method will enable design feasibility in building

hybrid multilayer optoelectronic devices such as solar cells, photodetectors and light-emitting diodes (LEDs), *etc*, which is of great benefit to the expansion of perovskite applications.

The diffusion-facilitated spatial confinement method is used to obtain large-area perovskite single-crystalline films with controllable thickness down to hundreds of nanometers.[23-26] In this process, the confined space was constructed by two SiO_2/Si substrates which were treated with octadecyltrichlorosilane (OTS) to realize a hydrophobic surface with lower surface energy. The contact angle measurements were carried out using the Owens and Wendt method with two different test liquids to evaluate the surface energy of untreated and OTS-treated SiO_2/Si substrates.[29,30] The contact angles measured with water and glycerol are 103.6° and 99.5° for untreated substrates, whereas 52.9° and 51.8° for OTS-treated substrates, as shown in **Figure S1**a, b. The surface energy of the untreated SiO_2/Si substrate is evaluated to be 47.57 mJ/m^2, and then decreases to 11.09 mJ/m^2 after OTS modification for the SiO_2/Si substrate. This low surface energy for the OTS-treated SiO_2/Si substrate is equivalent to the hydrophobic surface.[31] As noted in previous reports, the interaction between substrate surface and precursor solution will play a vital role in ion diffusion while the gap is limited down to the micrometer scale.[25] After OTS modification, ion diffusion is accelerated to enable a continuous crystallization growth of the perovskite single-crystalline films with a large area along an in-plane direction, as depicted in **Figure S1**c, d.[25] Schematic illustration of perovskite single-crystalline film growth process is shown in **Figure S2**a, in which a customized holder was utilized during the crystallization growth. First, a piece of OTS-treated SiO_2/Si substrate (1 cm × 1 cm) was put onto the other OTS-treated SiO_2/Si substrate (1 cm × 1 cm) to build up the narrow space. Then a droplet (0.6 μL) of supersaturated precursor solution was placed at the edge of the SiO_2/Si substrates which was gradually absorbed into the gap by capillarity. The supersaturation of precursor solution was prepared according to the inverse solubility method and described in the Experimental Section.[32-34] These substrates were then transferred to the center of the customized holder. The weight of the holder's cover was measured to be about

650 g which provided a pressure of about 64 kPa on the top of the SiO_2/Si substrates. Finally, this system was placed on a metal hot plate for about 24-36 hours to grow the perovskite single-crystalline films by inverse temperature crystallization until the crystallization growth completed.[32-34] Perovskite single-crystalline films were grown on one OTS-treated SiO_2/Si substrate and the other OTS-treated SiO_2/Si substrate can be easily detached.

Formamidinium lead halide perovskites ($FAPbX_3$) in which organic methylammonium cation (MA^+) is replaced with the larger formamidinium cation (FA^+) occupy the "A" site in the ABX_3 perovskite structure, are demonstrated to be a better optoelectronic material with better thermal stability and superior carrier transport characteristics than its methylammonium counterpart.[35,36] In terms of the perovskite single-crystalline films, most research efforts up to now are restricted to the investigation of the conventional methylammonium perovskites.[23-26] Formamidinium single-crystalline films are attempted in this work which is expected to provide more excitement in perovskite optoelectronic applications. **Figure 1**a shows the top-view photograph of a $FAPbBr_3$ single-crystalline film with a regular shape and a size of hundreds of micrometers. The scanning electron microscope (SEM) image in **Figure 1**b presents that the single-crystalline films also contain angled facets and smooth surfaces without visible grain boundaries and voids. The thickness of these perovskite single-crystalline films ranges from 100 to 300 nm, which exhibits characteristic colors observed by optical microscopy (**Figure S2**b). The clear thickness-dependent colors can be ascribed to the light interference effect.[23, 37, 38] This phenomenon can help us to determine the crystals with a certain thickness by direct visual inspection of the perovskite single-crystalline films. Here, the characterization of the crystal thickness was performed by the surface profiler. The photograph of the $FAPbBr_3$ single-crystalline films on the entire SiO_2/Si substrate (1 cm × 1 cm) with a size of millimeter level is shown in **Figure S3**. Atomic force microscopy (AFM) image of a $FAPbBr_3$ single-crystalline film also displays desirable surface homogeneity and sharp edges (**Figure 1**d). At the crystal

edge, steps can be clearly observed which is measured to be a height of 6.0 Å (**Figure 1**e, f), corresponding to a single monolayer of a cubic $FAPbBr_3$ unit cell (**Figure 1**c).[39, 40]

The obtained single-crystalline films are fixed on the SiO_2/Si substrate which will render these perovskite single-crystalline samples impractical for hybrid multilayer optoelectronic devices. Thus, transferring perovskite single-crystalline films onto other functional materials or substrates is strongly relevant for fundamental studies and even the optimization of perovskite's device performance. A wet transfer method is carried out for transferring perovskite single-crystalline films onto different substrates which is similar to the previously used strategy for the graphene transfer.[41,42] **Figure 2**a summarizes the steps of this wet transferring process. A polymer layer of polystyrene (PS) (0.15 g/mL in toluene) was spin-coated onto perovskite single-crystalline films grown on the OTS-treated SiO_2/Si substrate prior to the transfer. Afterwards, the detachment of the PS/perovskite layer from the initial surface can be easily done without any further treatment. Manual peeling was used to detach completely the PS/perovskite membrane from the substrate, which can be attributed to the hydrophobic surface of OTS-treated SiO_2/Si substrate with lower surface energy.[31] Finally, this membrane was laid over the target substrate, and then the PS polymer was dissolved carefully with a slow toluene flow which is heated to 65 °C. Toluene is chosen in this transferring process because it is a less polar solvent which hardly dissolve perovskite materials.[18,43,44] In previous reports, toluene was usually used to promote nucleation during the perovskite crystallization as called solvent engineering.[18,43,44] Apparently, the morphology of the perovskite single-crystalline films is sustained without any destruction as shown in **Figure 2**b. Quantitative surface analysis was also conducted by AFM surface scan to investigate the solvent influence. As expected, the surface roughness with low root-mean-square (RMS) values is remained at the same level before and after transfer which are shown in **Figure S4**a-c. Our AFM analysis suggests that almost no morphological changes are induced by this transferring process. Importantly, this wet transfer method is universally applicable to various perovskites like MA- and Cs-based perovskite

single-crystalline films. **Figure S5** shows the flowchart of the transferring process for $MAPbI_3$ single-crystalline films. According to the observation in the photographs, millimeter-sized $MAPbI_3$ single-crystalline films have been *in situ* grown on the OTS-treated SiO_2/Si substrate (**Figure S5**a). After spin-coated by a thin PS polymer film (**Figure S5**b), $MAPbI_3$ single-crystalline films can be completely transferred to a glass substrate (**Figure S5**c). $MAPbI_3$ and $CsPbBr_3$ single-crystalline films display uniform crystalline morphologies before and after transfer process, which are similar to that of $FAPbBr_3$, as seen in optical images (**Figure S6**). It is noted that the morphology profiles of perovskite single crystals are related to their crystallographic system to some extent.[23,32] Different from cubic $FAPbBr_3$ single-crystalline films with well-defined right angular edges, the tetragonal $MAPbI_3$ crystals usually show the edges with oblique angles.[23] These results demonstrate that this wet transfer method can be used as a general approach to transfer perovskite single-crystalline films for further device integration.

Most intriguingly, we found that perovskite single-crystalline films can be transferred to a variety of flat substrates, including silicon wafer, glass, sapphire and Au-coated SiO_2/Si substrate, etc. This substrate-independent behavior provides a new and convenient variable for fundamental studies on perovskite's photophysical properties. Then the optical properties of thin $FAPbBr_3$ single-crystalline films can be investigated after transferred to the glass substrate. **Figure 3**a shows the steady-state absorption and photoluminescence (PL) spectra of $FAPbBr_3$ single-crystalline films. A clear absorption onset is observed at the wavelength of 554 nm, corresponding to a bandgap of 2.26 eV as extracted from the Tauc plot of the absorption spectrum (**Figure 3**b).[45-48] The narrow PL peak at 547 nm is shorter than the absorption onset, indicating that the PL emission can be extinguished by themselves which has been reported before.[45-48] The X-ray diffraction (XRD) patterns in **Figure 3**c reveal a typical cubic lattice with the space group *Pm-3m* of the $FAPbBr_3$ single-crystalline films.[33] There are only three major diffraction peaks which can be assigned to (001), (002) and (003) planes, indicating that

the crystal film is (001) oriented.[33] Furthermore, the XRD patterns of $FAPbBr_3$ bulk crystal confirm the cubic crystalline structure of these single-crystalline thin films. Raman experiments performed on $FAPbBr_3$ single-crystalline films also benefit from this transferring process. Similarly, the analyses on the XRD patterns of thin $MAPbI_3$ and $CsPbBr_3$ single-crystalline films are shown in **Figure S7**. The sharp diffraction peaks observed from $MAPbI_3$ and $CsPbBr_3$ single-crystalline films illustrate that they have tetragonal and orthorhombic crystal structure, respectively, which are consistent with previous results.[32-34] **Figure S8**a shows the Raman spectrum measured for $FAPbBr_3$ single-crystalline films on SiO_2/Si substrate in the range of Raman shift from 200 to 1200 cm^{-1}. It is visible that the contribution of silicon line '520 cm^{-1}' strongly influences the measured spectrum.[49] The band placed between 930 and 1030 cm^{-1} is assigned to multi-phonon scattering coming from silicon substrate.[49] There are no characteristic vibration bands coming from $FAPbBr_3$ single-crystalline films as shown in **Figure S8**a which are totally covered by the contribution of silicon line '520 cm^{-1}'. However, after transferred to the sapphire substrate, the Raman bands of $FAPbBr_3$ single-crystalline films can be recognized in the spectrum of **Figure 3**d. The band near 521 cm^{-1} is assigned to the bending H_2N-C-NH_2 modes, and the band near 1120 cm^{-1} is assigned to symmetric stretching C-N modes.[47,48] The typical Raman spectrum of sapphire substrate is presented as the reference in **Figure S5**b. Then, the existence of the band located at 414 cm^{-1} in **Figure 3**d can be assigned to vibrations from sapphire substrate.[50] Transmission electron microscope (TEM) was also used to characterize $FAPbBr_3$ single-crystalline films as shown in **Figure 3**e. The samples can be prepared by transferring the single-crystalline films onto the TEM grid instead of substrate. **Figure 3**d shows the selected-area electron diffraction (SAED) pattern of $FAPbBr_3$ single-crystalline films with bright and sharp spots, confirming good single-crystalline quality. Furthermore, the chemical compositions of $FAPbBr_3$ single-crystalline films were tested by scanning TEM (STEM)-energy dispersion spectrum (EDS) elemental mapping, as shown in **Figure S9**a, b. It is visible that C, N, Pb and Br elements are uniformly distributed in $FAPbBr_3$

single-crystalline films, implying the high uniformity of the product. And the EDX analysis depicts a Pb/Br atomic ratio of 1:2.94 (**Figure S9**c), which is in good agreement with the 1:3 stoichiometry of $FAPbBr_3$.[33]

This wet transfer method will bring appealing potentials to incorporate perovskite single-crystalline films into multilayer optoelectronic devices and widen the range of their applications. In order to prove the technical potential, photodetectors have been fabricated with a coplanar metal-semiconductor-metal configuration by direct transferring $FAPbBr_3$ single-crystalline films onto patterned interdigital Au electrodes. A photograph of the device is shown in **Figure 4**a. The width of the gaps between neighboring digits is 10 μm, and the size of the $FAPbBr_3$ single-crystalline films used for photodetectors is regulated to around 0.2 mm^2. The energy band diagram of the Au/$FAPbBr_3$/Au structure demonstrates the processes of generation, transfer and collection of the photogenerated carriers (**Figure 4**b). Under illumination, electron-hole pairs are generated by absorbing light in the $FAPbBr_3$ perovskites, and then rapidly separated by the internal electric field towards the opposite contact electrodes.[51] The time-resolved PL of the $FAPbBr_3$ single-crystalline films was measured in nanosecond time scale through a time-correlated single photo counting system (TCSPC). As shown in **Figure 4**c, the decay curve of transient state PL measured at 540 nm can be deducted via a two-exponential fitting with an average PL decay lifetime of about 151 ns, implying a low concentration of trap states inside $FAPbBr_3$ single-crystalline films.[35] This relatively long radiative lifetime will be of great benefit to the $FAPbBr_3$ single-crystalline film-based photodetectors which guarantees to collect and transport more photogenerated carriers.[51] We note that Schottky barriers will be formed due to the weak contact between the $FAPbBr_3$ single-crystalline films and the interdigital electrodes where they are bonded via Van der Waals force.[35,51] However, a small external bias voltage can effectively compensate for this energy barrier. While the bias applying to the photodetector, ion migration together with carrier trapping will occur not only inside the

perovskite bulk but also at the interface of perovskite/electrode, which will give rise to an Ohmic contact.[35,51]

For the photodetector test, monochromatic LEDs were used as the light source with controlled light intensity. The photocurrent-voltage characteristics of the $FAPbBr_3$ single-crystalline film-based photodetector were performed under dark condition and 420 nm light illumination with varying light intensities **(Figure 4**d). As shown in **Figure 4**e, the current drastically increases with increacing incident light intensity, revealing a relation that the number of photogenerated carriers is proportional to the absorbed photon flux. The dark current is only 0.11 nA operated at 5 V bias, in contrast, the photocurrent reaches up to 212 nA at the light intensity of 970 μW cm^{-2}. The ultra-low dark current demonstrates the low carrier concentration of the $FAPbBr_3$ single-crystalline films and predicts high on/off photocurrent ratio. Then, it can be obtained of about 2×10^3 implying a high light switching behavior of the $FAPbBr_3$ single-crystalline film-based photodetectors. The periodic photoresponses of the photodetector were also characterized at the light intensity of 540 μW cm^{-2} under 5 V bias, with the light switched on and off for five cycles. A reproducible photocurrent response with good cycling stability can be observed from **Figure 4**f. Besides, we also measure the periodic photoresponses at different light intensities changing from 540 to 100 and 34 μW cm^{-2} with the bias maintained at 5 V (**Figure S10**a). And **Figure S10**b shows the periodic photoresponses measured using a series of bias voltages from 5 to 3 and 1 V. Each curve verifies a good repeatability and stable photocurrents.

Photoresponsivity (R) is defined as the ratio of photocurrent to incident light intensity, which can be expressed as:[52]

$$R = \frac{I_{light} - I_{dark}}{P_0 \cdot A} \quad (1)$$

where I_{light} is the photocurrent, I_{dark} is the dark current, P_0 is the incident light intensity, and A is the effective illumination area (half of the crystal area in this case). The photoresponsivity

corresponding to the incident light intensity under 420 nm light illumination at a bias of 5 V is plotted in **Figure 5**a with the highest value of 3.32 A W^{-1} at 0.03 μW cm^{-2}. Upon increasing the light illumination power to 34 μW cm^{-2} and above, the photoresponsivity decays and finally plateaus at a value around 0.22 A W^{-1}. The other two parameters, specific detectivity (D^*) and external quantum efficiency (EQE), are also crucial for photodetectors, which can be calculated using the equations:[52]

$$D^* = \frac{R\sqrt{A}}{\sqrt{2eI_{dark}}} \quad (2)$$

$$EQE = R\frac{hc}{e\lambda} \quad (3)$$

where e is the electronic charge, h is Planck's constant, c is the velocity of the incident light, and *),* is the wavelength of the incident light. Due to the large photoresponsivity R and relatively low dark current I_{dark}, the highest value of D^* and EQE are estimated to be 2.67×10^{12} Jones (1 Jones = 1 cm $Hz^{1/2}$ W^{-1}) and 982%, receptively, at a bias of 5 V. **Figure S10**c plots both D^* and EQE as a function of incident light intensity under 420 nm light illumination. It is obvious that both the specific detectivity and external quantum efficiency decrease with the increase of light intensity at weak light illumination. The same evolution as photoresponsivity is found that these two parameters keep nearly constant values when the light intensity reaches 34 μW cm^{-2}. In order to evaluate the selectivity of the $FAPbBr_3$ single-crystalline film-based photodetector to light illumination, the wavelength-dependent light response is measured with other four LEDs at the wavelengths of 370, 530, 598 and 685 nm. **Figure 5**b shows the photocurrent variation of the sample biased by varied voltages under different light illumination. The photodetector exhibits a broad photoresponse range from 370 to 530 nm, matching with the absorption spectrum (**Figure 5**c). For the response time measurement, we use a function generator that can generate a 50% duty cycle square waveform with a fast rise and fall time to switch the incident light, and the photocurrent signals are recorded using a low noise current preamplifier connecting to an oscilloscope. As shown below in **Figure 5**d, the rise time of the photodetector

(from 10% to 90% of the saturated value) is measured to be 115.2 ms, whereas the fall-time (from 90% to 10% peak value) is 198.4 ms. Meanwhile, the long-term operational stability of $FAPbBr_3$ single-crystalline film-based photodetector was also characterized, which has been recognized as a great challenge for organic-inorganic hybrid perovskites because of their poor stability against environmental oxygen/moisture. The photocurrent of the unencapsulated device exhibits high stability with little loss in responsivity after being stored for one week at the same light intensity of 540 $\mu W\ cm^{-2}$ under 5 V bias (**Figure S10**d). The high-performance achieved in the $FAPbBr_3$ single-crystalline film-based photodetectors can be attributed to the preserved perovskite single-crystalline morphologies with good qualities after the wet transferring process.

In conclusion, we report an improved diffusion-facilitated spatial confinement method for the scalable growth of perovskite single-crystalline films with hundreds of nanometers. The key is to introduce a hydrophobic surface with lower surface energy into the crystallization process, which can significantly accelerate the ion diffusion and enable the realization of continuous crystallization growth. With this method, millimeter-sized formamidinium lead halide perovskite ($FAPbBr_3$) single-crystalline films can be controllably prepared, which are expected to be superior optoelectronic material than conventional methylammonium counterpart. After that, a wet transfer method is developed to perfectly transfer these $FAPbBr_3$ single-crystalline films onto almost arbitrary substrates. Thanks to the hydrophobic layer modification, the $FAPbBr_3$ single-crystalline films can be easily peeled off from the original substrates without any destruction. Further studies reveal that the perovskite single-crystalline films sustain high crystalline quality and morphology after the transferring process. Then the $FAPbBr_3$ single-crystalline films are directly transferred onto patterned interdigital Au electrodes for the fabrication of photodetectors, exhibiting a remarkable photoresponsivity with a high responsivity of 3.32 $A\ W^{-1}$. This wet transfer method provides a scalable pathway to incorporate

perovskite single-crystalline films into multilayer devices for building efficient optoelectronic devices.

Experimental Section

Materials: All the reagents were used as received without further purification: Formamidinium bromide (FABr, Sigma-Aldrich), Methylammonium iodide (MAI, Sigma-Aldrich), Cesium bromide (CsBr, Sigma-Aldrich), Lead(II) bromide, ($PbBr_2$, TCI America), Lead(II) iodide, (PbI_2 , TCI America), *N,N*-dimethylformamide (DMF, anhydrous, 99%, Sigma-Aldrich), Dimethyl sulfoxide (DMSO, anhydrous, 99.9%, Sigma-Aldrich), y-Butyrolactone (GBL, analytical standard, Sigma-Aldrich), Toluene (Tol, 99%, Alfa), Octadecyltrichlorosilane (OTS, 90%, Sigma-Aldrich), Polystyrene (PS, average M_w~35,000, Sigma-Aldrich).

Substrate Preparation: The silicon wafer, glass, sapphire, SiO_2/Si, and Au-coated SiO_2/Si substrates were rinsed with acetone, ethanol, and deionized water by ultrasonic bath for 15 mins and dried with quick purged N_2 flow. The SiO_2/Si substrates were treated by an oxygen plasma cleaner at 300 W for 7 mins. The substrates with a layer of interdigital Au electrodes were purchased from MECART Corp. and used without further treatment after removing the protecting films. OTS modification was carried out on the plasma cleaned SiO_2/Si substrates by the vapor deposition method to realize a hydrophobic surface, which was placed inside a vacuum drying oven at 65 °C for about 5 h.

Crystallization Growth: The perovskite single-crystalline films were grown by a diffusion-facilitated spatial confinement method. The OTS-treated substrates were transferred to a nitrogen glove box (below 0.1 ppm O_2 and 0.1 ppm H_2O). The perovskite supersaturated precursor solutions were prepared as below: $FAPbBr_3$ (FAPb:$PbBr_2$ = 1:1 molar ratio) resolved in mixture of GBL and DMF (3:2) at 1 M concentration; $MAPbI_3$ (MAPb:PbI_2 = 1:1 molar ratio) resolved in GBL at 1.2 M concentration; $CsPbBr_3$ (CsBr:$PbBr_2$ = 1:2 molar ratio) resolved in DMSO at 1 M concentration of Pb.[32-34] A droplet (0.6 μL) of supersaturated precursor

solution was then injected at the edge of the sandwiched OTS-treated substrates and absorbed into the gap through capillary force. Crystal growth was achieved by placing the customized holder on a hot plate for about 24-36 h and annealing at a fixed temperature of 65 °C, 135 °C, and 60 °C for $FAPbBr_3$, $MAPbI_3$, and $CsPbBr_3$, respectively.[32-34]

Device Fabrication: The perovskite single-crystalline film-based photodetectors can be fabricated by direct transferring perovskite single-crystalline films onto patterned interdigital Au electrodes through the wet transfer method.[41,42] A layer of polystyrene (PS) was deposited onto the single-crystalline film surface by spin-coating at 2000 rpm for 30 s, respectively. The PS/perovskite membrane was then laid over the interdigital Au electrodes which was similar to pasting a screen protector film. Afterwards, the PS layer was removed by dissolving in heated (65 °C) toluene for 2 mins. The perovskite single-crystalline film-based photodetectors were characterized using a semiconductor parameter analyzer (Keithley 4200) under light illumination at various intensities and wavelengths in the nitrogen glove box. The light sources for this work were LEDs with the wavelengths of 370, 420, 530, 598 and 685 nm. When measuring the spectral responsivity, the intensity at all measured wavelengths was set to be about 540 μW cm^{-2}. The response time of the photodetector was measured using a function generator which can generate a 50% duty cycle square waveform with fast rise and fall time to switch the incident light, and the photocurrent signals were recorded using a low noise current preamplifier (Stanford Research Systems SR570) connecting to a digital storage oscilloscope (LeCroy WaveRunner Oscilloscope 44MXI).

Characterization: The structural information of the perovskite single-crystalline films was characterized by X-ray diffraction using a Rigaku SmartLab (Rigaku, Japan) with Cu Ka radiation (. = 0.15406 nm). The morphology of the perovskite single-crystalline films was characterized by atomic force microscopy (AFM, Asylum MFP-3D Infinity), field emission scanning electron microscopy (SEM, JEOL Model JSM-6490) and scanning transmission

electron microscopy (STEM, JEOL Model JEM-2100F) with an energy dispersive X-ray (EDX, Oxford Instrument) spectrometry system. The absorbance spectra were measured using a UV-vis spectrophotometer (UV-3600, Hitachi). A TCSPC system was equipped with a 379 nm picosecond diode laser (Edinburgh Instruments EPL375, repetition rate 20 MHz) to excite the sample. The emission was detected using a spectrophotometer (Edinburgh FLSP920). The Raman spectra were obtained from a Witec Confocal Raman system equipped with an excitation source of continuous-wave 633 nm laser diode. The contact angle (CA) was measured using a Contact Angle System OCA 20 instrument (DataPhysics Instruments GmbH, Germany). The thickness of the perovskite single-crystalline films was determined by a surface profiler (Bruker DektakXT).

Supporting Information

Supporting Information is available from the Wiley Online Library or from the author.

Acknowledgements

The authors gratefully acknowledge the financial support from the Hong Kong Scholars Program (Grant No. XJ2018004), and the Research Grants Council of Hong Kong (GRF No. PolyU 153023/18P).

Received: ((will be filled in by the editorial staff))
Revised: ((will be filled in by the editorial staff))
Published online: ((will be filled in by the editorial staff))

References

[1] G. C. Xing, N. Mathews, S. Y. Sun, S. S. Lim, Y. M. Lam, M. Grätzel, S. Mhaisalkar, T. C. Sum, *Science* **2013**, *342*, 344.

[2] S. D. Stranks, G. E. Eperon, G. Grancini, C. Menelaou, M. J. P. Alcocer, T. Leijtens, L. M. Herz, A. Petrozza, H. J. Snaith, *Science* **2013**, 342, 341.

[3] M. A. Green, A. Ho-Baillie, H. J. Snaith, *Nat. Photonics* **2014**, 8, 506.

[4] H. Zhou, Q. Chen, G. Li, S. Luo, T.-b. Song, H.-S. Duan, Z. Hong, J. You, Y. Liu, Y. Yang, *Science* **2014**, 345, 542.

[5] Q. Dong, Y. Fang, Y. Shao, P. Mulligan, J. Qiu, L. Cao, J. S. Huang, *Science* **2015**, *347*, 967.

[6] D. Shi, V. Adinolfi, R. Comin, M. Yuan, E. Alarousu, A. Buin, Y. Chen, S. Hoogland, A. Rothenberger, K. Katsiev, Y. Losovyj, X. Zhang, P. A. Dowben, O. F. Mohammed, E. H. Sargent, O. M. Bakr, *Science* **2015**, *347*, 519.

[7] W. Y. Nie, H. H. Tsai, R. Asadpour, J. C. Blancon, A. J. Neukirch, G. Gupta, J. J. Crochet, M. Chhowalla, S. Tretiak, M. A. Alam, H. L. Wang, A. D. Mohite, *Science* **2015**, 347, 522.

[8] X. Li, D. Bi, C. Yi, J.-D. Décoppet, J. Luo, S. M. Zakeeruddin, A. Hagfeldt, M. Grätzel, *Science* **2016**, 353, 58.

[9] S. S. Shin, E. J. Yeom, W. S. Yang, S. Hur, M. G. Kim, J. Im, J. Seo, J. H. Noh, S. I. Seok, *Science* **2017**, *356*, 167.

[10] R. Ding, X. Zhang, X. W. Sun, *Adv. Funct. Mater.* **2017**, *27*, 1702207.

[11] A. Ng, Z. Ren, Q. Shen, S. H. Cheung, H. C. Gokkaya, G. Bai, J. Wang, L. Yang, S. K. So, A. B. Djurisic, W. W. Leung, J. Hao, W. K. Chan, C. Surya, *J. Mater. Chem. A* **2015***, 3*, 9223.

[12] P. -L. Qin, G. Yang, S. H. Cheung, S. K. So, L. Chen, J. Hao, J. Hou, G. Li, *Adv. Mater.* **2018**, *30*, 1706126.

[13] Z. Ren, A. Ng, Q. Shen, H. C. Gokkaya, J. Wang, L. Yang, W. -K. Yiu, G. Bai, A. B. Djurisic, W. W. Leung, J. Hao, W. K. Chan, C. Surya, *Sci. Rep.* **2014**, *4*, 6752.

[14] M. Abdi-Jalebi, Z. Andaji-Garmaroudi, S. Cacovich, C. Stavrakas, B. Philippe, J. M. Richter, M. Alsari, E. P. Booker, E. M. Hutter, A. J. Pearson, S. Lilliu, T. J. Savenije, H. Rensmo, G. Divitini, C. Ducati, R. H. Friend, S. D. Stranks, *Nature* **2018**, *555*, 497.

[15] E. H. Jung, N. J. Jeon, E. Y. Park, C. S. Moon, T. J. Shin, T.-Y. Yang, J. H. Noh, J. Seo, *Nature* **2019**, *567*, 511.

[16] S. Yang, S. Chen, E. Mosconi, Y. Fang, X. Xiao, C. Wang, Y. Zhou, Z. Yu, J. Zhao, Y. Gao, F. De Angelis, J. Huang, *Science* **2019**, *365*, 473.

[17] National Renewable Energy Laboratory, Best Research-Cell Efficiency Chart, https://www.nrel.gov/pv/cell-efficiency.html (accessed: August 2019)

[18] N. J. Jeon, J. H. Noh, Y. C. Kim, W. S. Yang, S. Ryu, S. I. Seok, *Nat. Mater.* **2014**, *13*, 897.

[19] Y. Deng, E. Peng, Y. Shao, Z. Xiao, Q. Dong, J. Huang, *Energy Environ. Sci.* **2015**, *8*, 1544.

[20] F. Ye, H. Chen, F. Xie, W. Tang, M. Yin, J. He, E. Bi, Y. Wang, X. Yang, L. Han, *Energy Environ. Sci.* **2016**, *9*, 2295.

[21] I. A. Shkrob, T. W. Marin, *J. Phys. Chem. Lett.* **2014**, *5*, 1066.

[22] N. K. Noel, A. Abate, S. D. Stranks, E. S. Parrott, V. M. Burlakov, A. Goriely, H. J. Snaith, *ACS Nano* **2014**, *8*, 9815.

[23] Y. -X. Chen, Q. -Q. Ge, Y. Shi, J. Liu, D. -J. Xue, J. -Y. Ma, J. Ding, H. -J. Yan, J. -S. Hu, L. -J. Wan, *J. Am. Chem. Soc.* **2016**, *138*, 16196.

[24] Z. Yang, Y. Deng, X. Zhang, S. Wang, H. Chen, S. Yang, J. Khurgin, N. X. Fang, X. Zhang, R. Ma, *Adv. Mater.* **2018**, *30*, 1704333.

[25] Z. Chen, Q. Dong, Y. Liu, C. Bao, Y. Fang, Y. Lin, S. Tang, Q. Wang, X. Xiao, Y. Bai, Y. Deng, J. Huang, *Nat. Commun.* **2017**, *8*, 1890.

[26] W. Yu, F. Li, L. Yu, M. R. Niazi, Y. Zou, D. Corzo, A. Basu, C. Ma, S. Dey, M. L. Tietze, U. Buttner, X. Wang, Z. Wang, M. N. Hedhili, C. Guo, T. Wu, A. Amassian, *Nat. Commun.* **2018**, *9*, 5354.

[27] L. Qin, B. Kattel, T. R. Kafle, M. Alamri, M. Gong, M. Panth, Y. Hou, J. Wu, W. -L. Chan, *Adv. Mater. Interfaces* **2019**, *6*, 1801419.

[28] X. Shen, M. Wang, F. Zhou, B. Qiu, L. Cai, Y. Liu, Z. Zheng, Y. Chai, *J. Mater. Chem. C* **2018**, *6*, 8663.

[29] D. K. Owens, R. C. Wendt, *Jour. of Applied Polymer Science* **1969**, *13*, 1741.

[30] R. J. Good, L. A. Girifalco, *J. Phys. Chem.* **1960**, *64*, 561.

[31] R. Ding, J. Feng, X. L. Zhang, W. Zhou, H. H. Fang, Y. F. Liu, Q. D. Chen, H. Y. Wang, H. B. Sun, *Adv. Funct. Mater.* **2014**, *24*, 7085.

[32] M. I. Saidaminov, A. L. Abdelhady, B. Murali, E. Alarousu, V. M. Burlakov, W. Peng, I. Dursun, L. Wang, Y. He, G. Maculan, A. Goriely, T. Wu, O. F. Mohammed, O. M. Bakr, *Nat. Commun.* **2015**, *6*, 7586.

[33] A. A. Zhumekenov, M. I. Saidaminov, M. A. Haque, E. Alarousu, S. P. Sarmah, B. Murali, I. Dursun, X. -H. Miao, A. L. Abdelhady, T. Wu, O. F. Mohammed, O. M. Bakr, *ACS Energy Lett.* **2016**, *1*, 32.

[34] D. N. Dirin, I. Cherniukh, S. Yakunin, Y. Shynkarenko, M. V. Kovalenko, *Chem. Mater*. **2016**, *28*, 8470.

[35] F. Zhang, B. Yang, K. Zheng, S. Yang, Y. Li, W. Deng, R. He, *Nano-Micro Lett.* **2018**, *10*, 43.

[36] Y. Liu, J. Sun, Z. Yang, D. Yang, X. Ren, H. Xu, Z. Yang, S. Liu, *Adv. Optical Mater.* **2016**, *4*, 1829.

[37] S.Roddaro, P. Pingue, V. Piazza, V. Pellegrini, F. Beltram, *Nano Lett.* **2007**, *7*, 2707.

[38] P. Blake, E. W. Hill, A. H. C. Neto, K. S. Novoselov, D. Jiang, R. Yang, T. J. Booth, A. K. Geim, *Appl. Phys. Lett.* **2007**, *91*, 063124.

[39] Y. Zhang, C. Wang, Z. Deng, *Chem. Commun.* **2018**, *54*, 4021.

[40] Y. Li, L. Han, Q. Liu, W. Wang, Y. Chen, M. Lyu, X. Li, H. Sun, H. Wang, S. Wang, Y. Li, *Nano Res.* **2018**, *11*, 3306.

[41] A. Reina, H. Son, L. Jiao, B. Fan, M. S. Dresselhaus, Z. F. Liu, J. Kong, *J. Phys. Chem. C* **2008**, *112*, 17741.

[42] E. H. Lock, M. Baraket, M. Laskoski, S. P. Mulvaney, W. K. Lee, P. E. Sheehan, D. R. Hines, J. T. Robinson, J. Tosado. M. S. Fuhrer, S. C. Hernández, S. G. Walton, *Nano Lett.* **2012**, *12*, 102.

[43] K. Kara, D. A. Kara, C. K1rb1y1k, M. Ersoz, 0. Usluer, A. L. Briseno, M. Kus, *RSC Adv.* **2016**, *6*, 26606.

[44] N. Sakai, S. Pathak, H. -W. Chen, A. A. Haghighirad, S. D. Stranks, T. Miyasaka, H. J. Snaith, *J. Mater. Chem. A* **2016**, *4*, 4464.

[45] F. Li, L. Yang, Z. Cai, K. Wei, F. Lin, J. You, T. Jiang, Y. Wang, X. Chen, *Nanoscale* **2018**, *10*, 20611.

[46] L. Protesescu, S. Yakunin, M. I. Bodnarchuk, F. Bertolotti, N. Masciocchi, A. Guagliardi, M. V. Kovalenko, *J. Am. Chem. Soc.* **2016**, *138*, 14202.

[47] L. A. T. Nguyen, D. N. Minh, Y. Yuan, S. Samanta, L. Wang, D. Zhang, N. Hirao, J. Kim, Y. Kang, *Nanoscale* **2019**, *11*, 5868.

[48] L. Wang, K. Wang, B. Zou, *J. Phys. Chem. Lett.* **2016**, *7*, 2556.

[49] P. Borowicz, M. Latek, W. Rzodkiewicz, A. Laszcz, A. Czerwinski, J. Ratajczak, *Adv. Nat. Sci.: Nanosci. Nanotechnol.* **2012**, *3*, 045003.

[50] M. Kadleíková, J. Breza, M. Veselý, *Microelectron. J.* **2001**, *32*, 955.

[51] L. Z. Lei, Z. -F. Shi, Y. Li, Z. -Z. Ma, F. Zhang, T. -T. Xu, Y. -T. Tian, D. Wu, X. -J. Li, G. -T. Du, *J. Mater. Chem. C* **2018**, *6*, 7982.

[52] C. Xie, C. -K. Liu, H. -L. Lo, F. Yan, *Adv. Funct. Mater.* **2019**, 1903907.

Figures and their captions

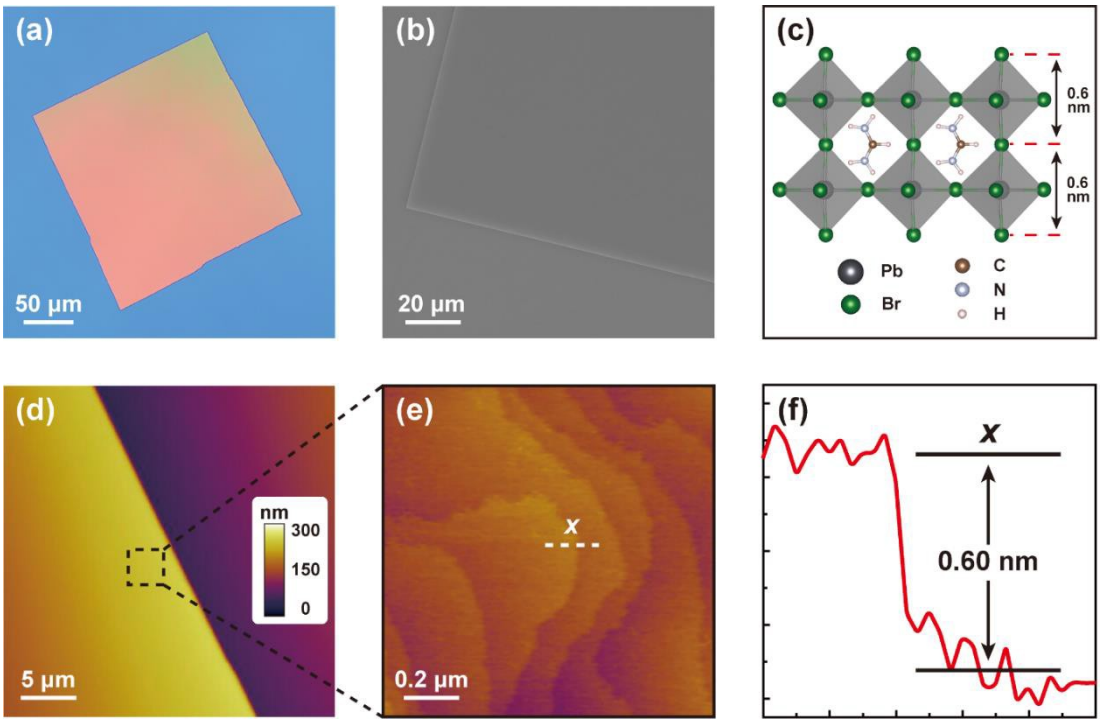

Figure 1. Characterization of $FAPbBr_3$ single-crystalline thin films. Top-view optical **a)** and SEM images **b)** of $FAPbBr_3$ single-crystalline films on SiO_2/Si substrate. **c)** Schematic representation of perovskite layered crystal structure. AFM images of $FAPbBr_3$ single-crystalline films **d)** and **e)** with monolayer height profile **f)**.

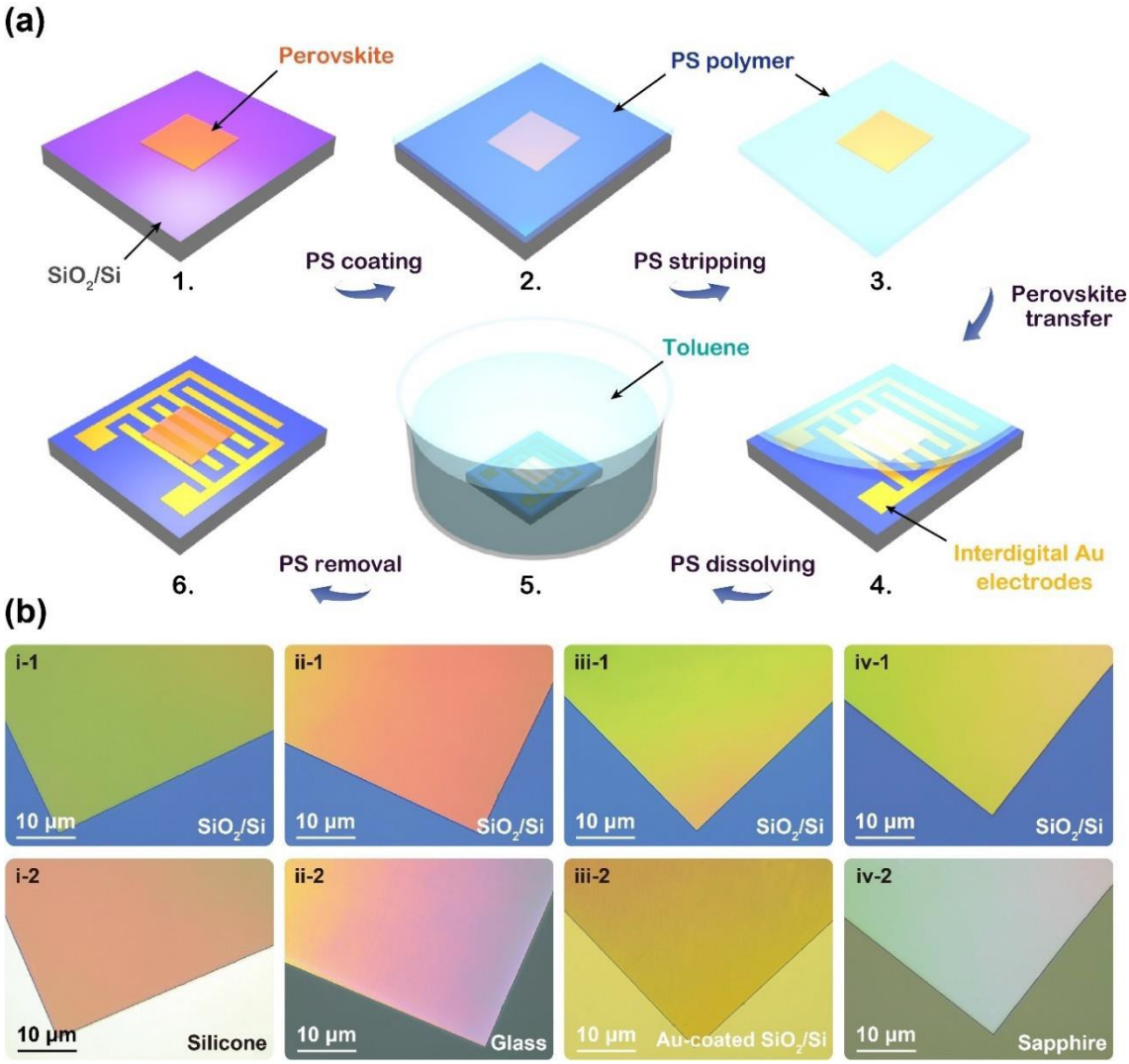

Figure 2. a) Schematic illustration of the wet transferring process. A perovskite single-crystalline film is grown on an OTS-treated SiO_2/Si substrate (step 1), and a PS polymer is spin-coated onto the crystal surface (step 2). Then the PS/perovskite layer can be peeled off from the SiO_2/Si substrate (step 3), and the PS/perovskite membrane is laid over the target substrate (step 4). After dissolved in a slow toluene flow (step 5), the perovskite single-crystalline film is successfully transferred to the target substrate for further applications (step 6). **b)** Optical images of $FAPbBr_3$ single-crystalline films on the original SiO_2/Si substrates (i-1, ii-1, iii-1 and iv-1) and transferred substrates (i-2: silicon wafer, ii-2: glass, iii-2: Au-coated SiO_2/Si substrate and iv-2: sapphire).

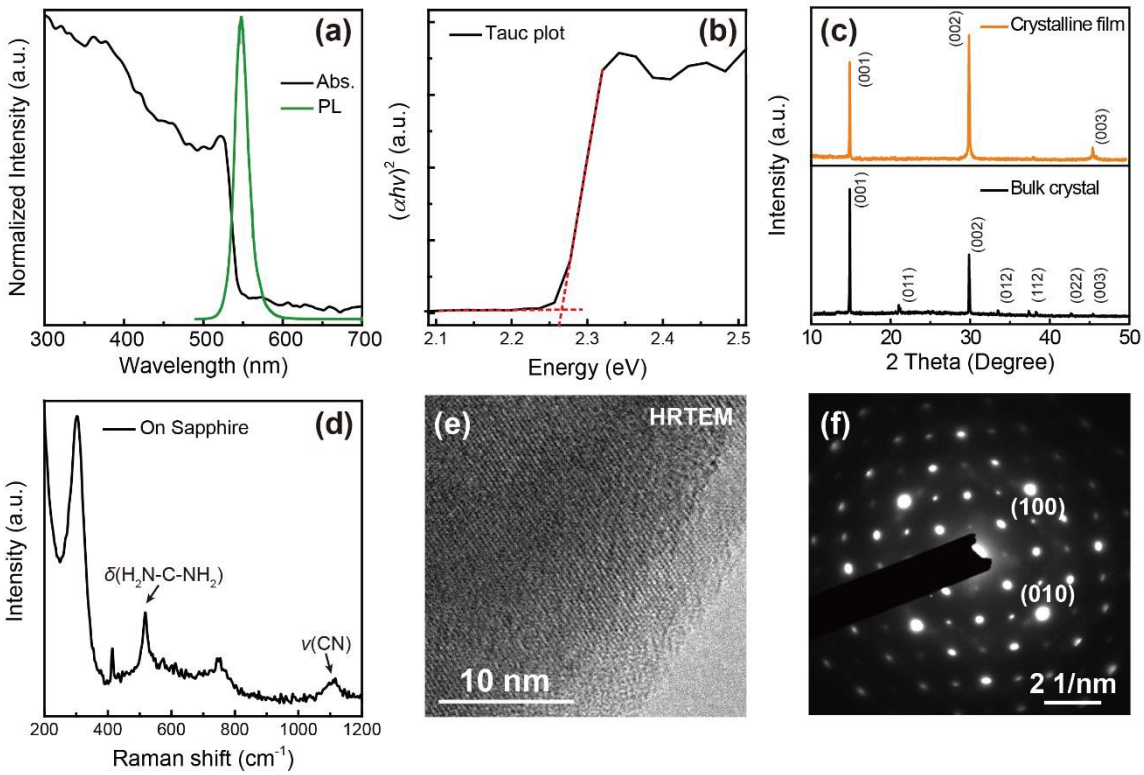

Figure 3. a) Steady-state absorption and PL spectra of $FAPbBr_3$ single-crystalline films. **b)** Optical bandgap of $FAPbBr_3$ single-crystalline films extracted from Tauc plot. **c)** XRD patterns of $FAPbBr_3$ single-crystalline films and $FAPbBr_3$ bulk crystals. **d)** Raman spectra measured for $FAPbBr_3$ single-crystalline films on sapphire substrate. **e)** TEM image and **f)** the corresponding SAED pattern of of $FAPbBr_3$ single-crystalline films.

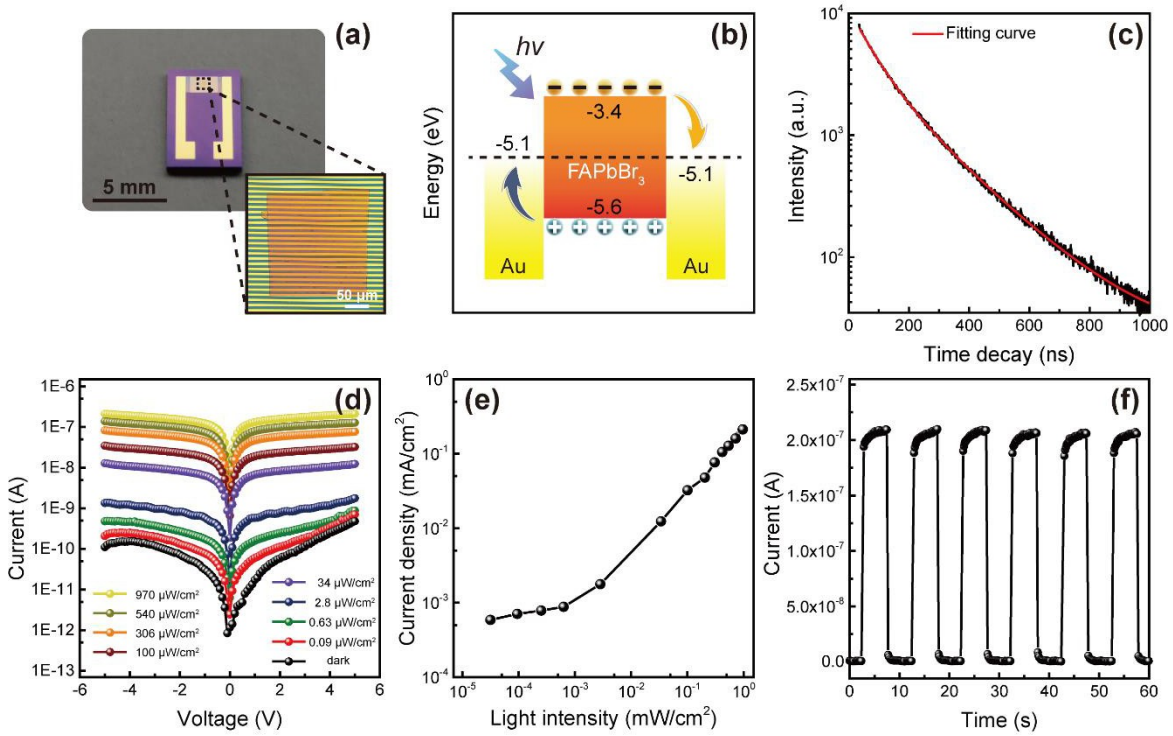

Figure 4. a) Photography of the photodetector based on $FAPbBr_3$ single-crystalline films. **b)** Energy band diagram of the Au/$FAPbBr_3$/Au structure illustrating the generation, transfer and collection processes of photogenerated carriers. **c)** Time-resolved PL decay and the corresponding fitting curve of the $FAPbBr_3$ single-crystalline films. **d)** The photocurrent-voltage characteristics of the photodetector performed under dark condition and 420 nm light illumination with varying light intensities. **e)** Intensity-dependent photocurrent with a bias of 5 V. **f)** Time-dependent photoresponse of the photodetector with good cycling stability measured at the light intensity of 540 μW cm^{-2} under 5 V bias.

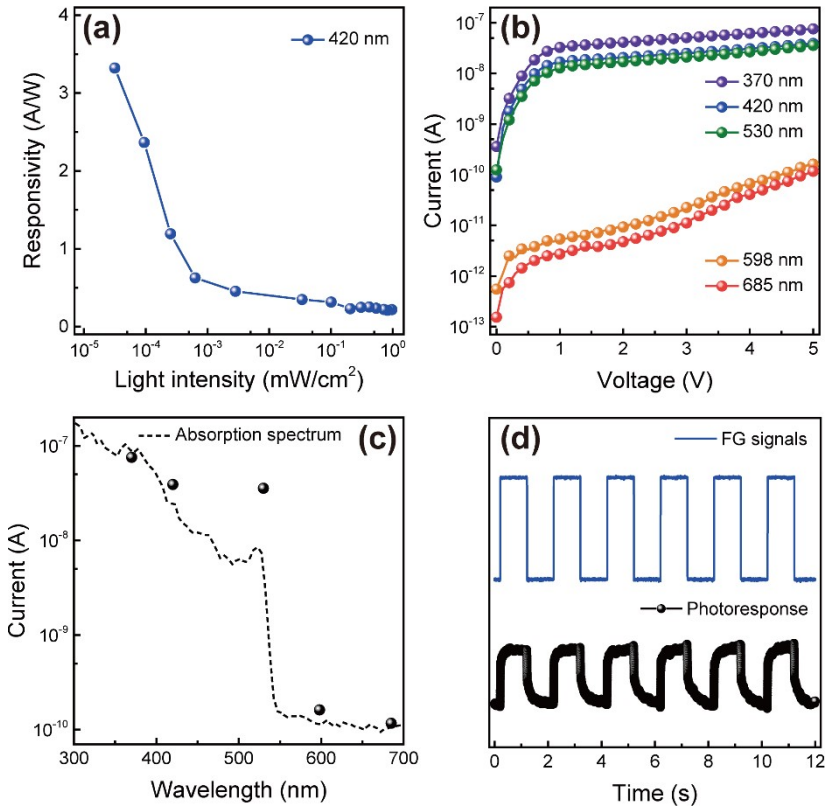

Figure 5. a) Photoresponsivity of the photodetector as a function of incident light intensity under 420 nm light illumination at a bias of 5 V. **b)** The photocurrent-voltage characteristics of the photodetector performed under different light illumination. **c)** Responsivity of the photodetector versus wavelength of the incident light. **d)** Response time measured with a monochromatic LED of 420 nm controlled by a function generator.

Large-area perovskite single-crystalline thin-films are perfectly transferred onto electrode substrates for photodetectors exhibiting remarkable photoresponsivity through a wet transfer method. This transferring strategy can be potentially used as a building block for incorporating perovskite single-crystalline films into multilayer devices for building efficient optoelectronic perovskite devices.

Keywords: (perovskite single-crystalline films, wet transfer method, $FAPbBr_3$, photodetectors)

Ran Ding, Chun-Ki Liu, Zehan Wu, Feng Guo, Sin-Yi Pang, Lok Wing Wong, Weng Fu Io, Shuoguo Yuan, Man-Chung Wong, Michal Bartlomiej Jedrzejczyk, Jiong Zhao, Feng Yan and Jianhua Hao*

A General Approach for Direct Wet Transfer of Large-Area Optoelectronic Hybrid Perovskite Single-Crystalline Thin-Films

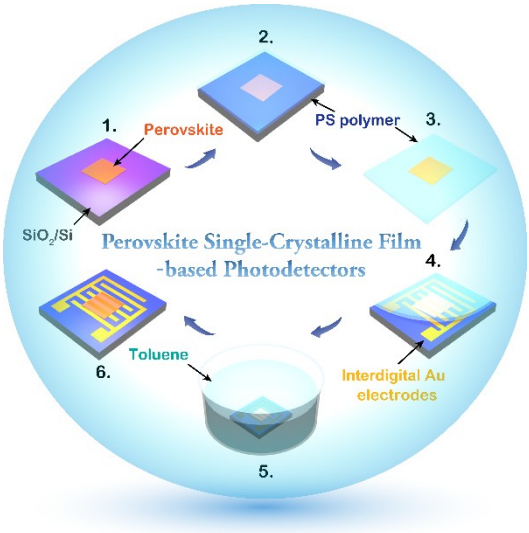

Supporting Information

A General Approach for Direct Wet Transfer of Large-Area Optoelectronic Hybrid Perovskite Single-Crystalline Thin-Films

*Ran Ding, Chun-Ki Liu, Zehan Wu, Feng Guo, Sin-Yi Pang, Lok Wing Wong, Weng Fu Io, Shuoguo Yuan, Man-Chung Wong, Michal Bartlomiej Jedrzejczyk, Jiong Zhao, Feng Yan and Jianhua Hao**

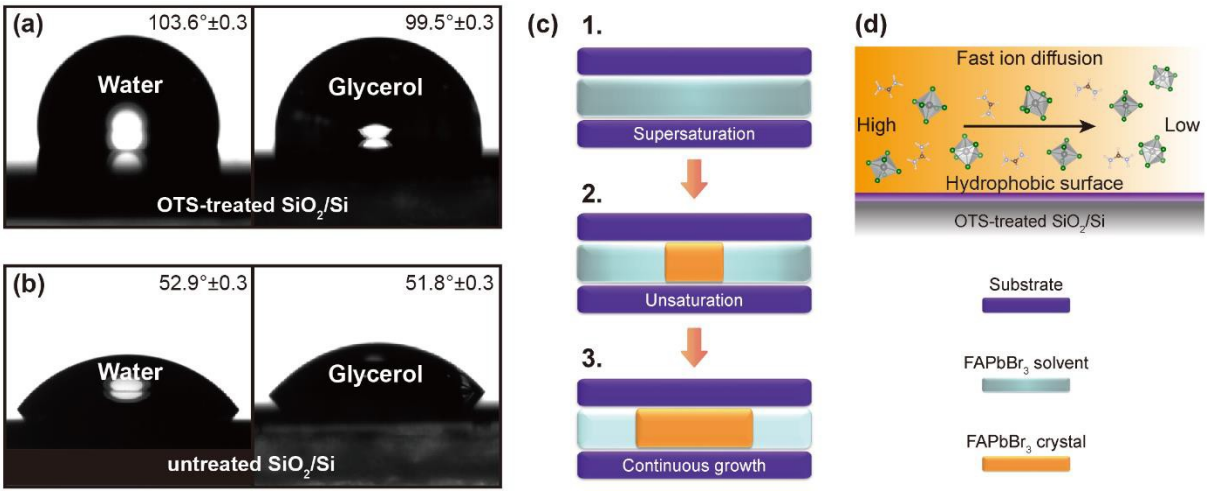

Figure S1. The images of contact angle measurements of OTS-treated SiO_2/Si substrate **a)** and untreated SiO_2/Si substrate **b)** with water and glycerol. Schematic illustration of correlation between ion diffusion and crystallization growth **c)** and ion diffusion rate on hydrophobic surface **d)**.

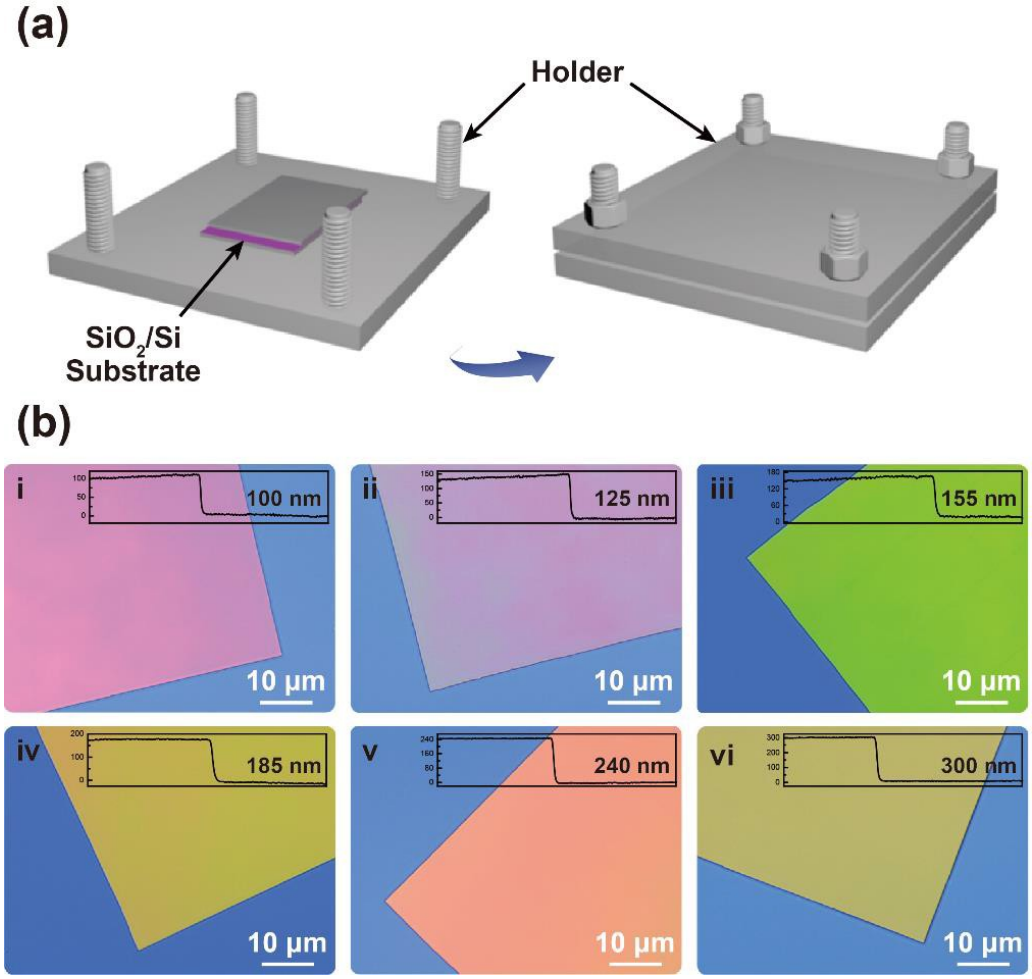

Figure S2. a) Schematic illustration of growth process with a customized holder. **b)** Top-view optical images of $FAPbBr_3$ single-crystalline films with certain thicknesses which show the thickness-dependent colors.

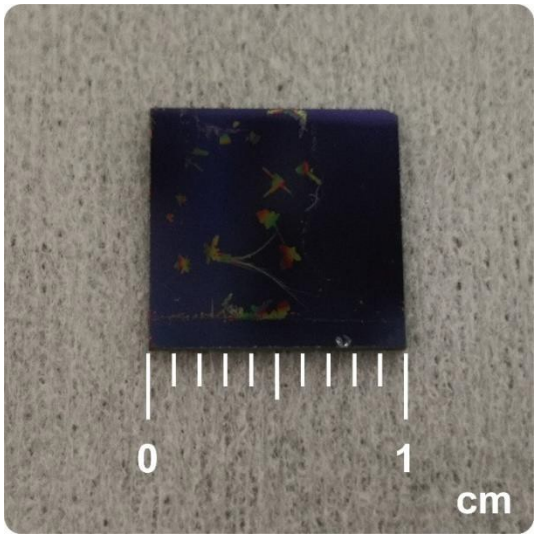

Figure S3. The photograph of the $FAPbBr_3$ single-crystalline films grown on the entire SiO_2/Si substrate (1 cm × 1 cm) with size of millimeter level.

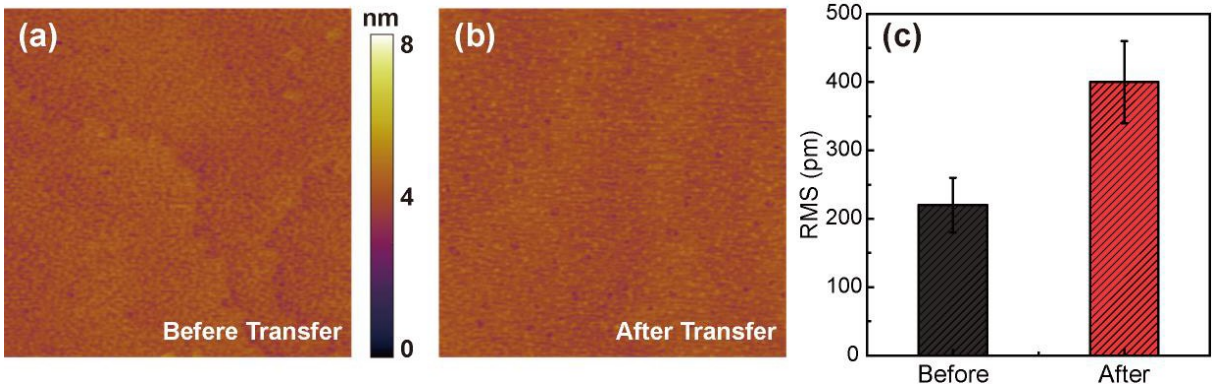

Figure S4. AFM surface images of $FAPbBr_3$ single-crystalline films before **a)** and after **b)** the transfer, and their corresponding root mean square roughness of the crystal surface within a 25 μm^2 area **c)**.

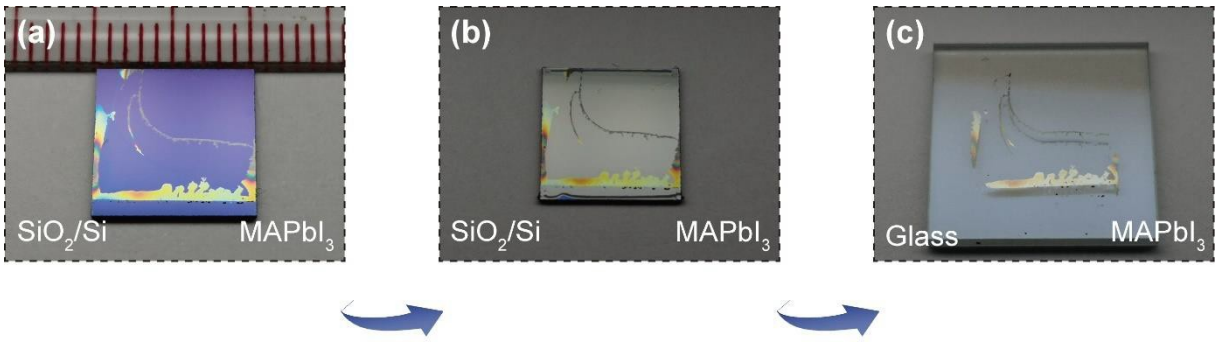

Figure S5. The flowchart of the transferring process for millimeter-sized $MAPbI_3$ single-crystalline films.

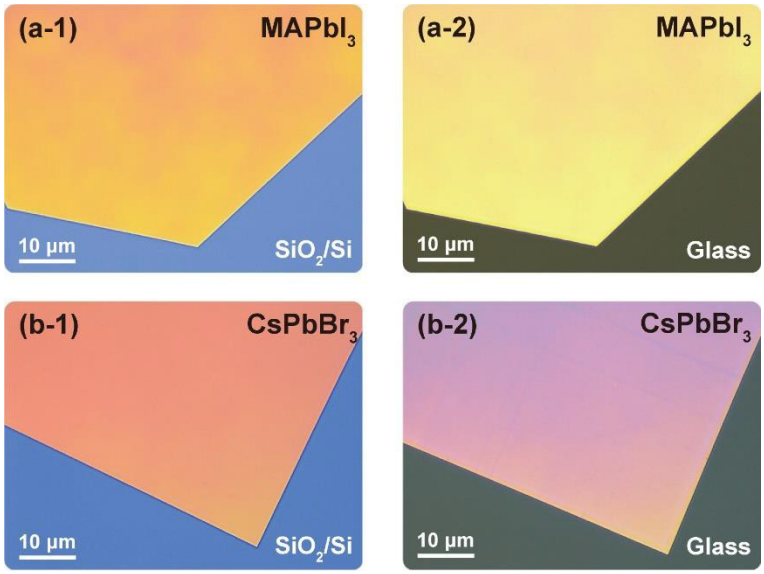

Figure S6. Optical images of $MAPbI_3$ **a)** and $CsPbBr_3$ **b)** single-crystalline films on the original SiO_2/Si substrates and transferred glass substrates.

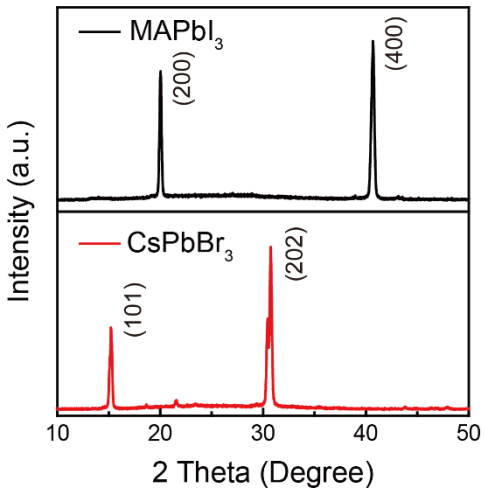

Figure S7. The measured XRD patterns of $MAPbI_3$ and $CsPbBr_3$ single-crystalline films.

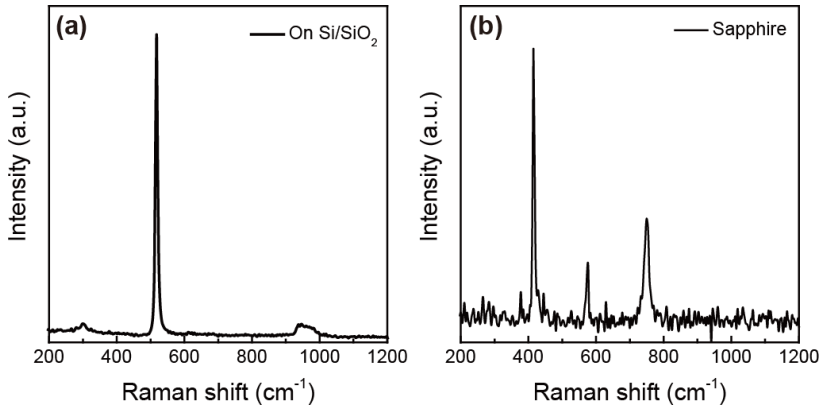

Figure S8. Raman spectra measured for $FAPbBr_3$ single-crystalline films on SiO_2/Si substrate **a)** and sapphire substrate **b)**.

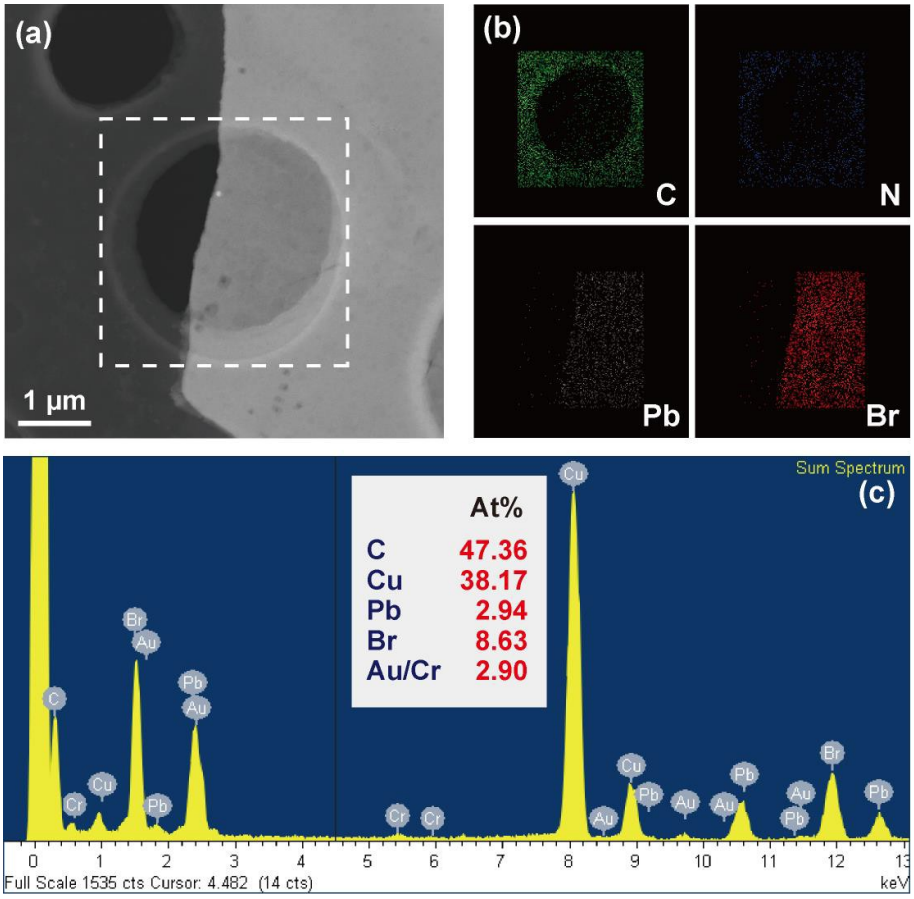

Figure S9. STEM image **a)**, the corresponding STEM-EDS elemental mappings **b)** and estimated atomic ratio of $FAPbBr_3$ single-crystalline films **c)**.

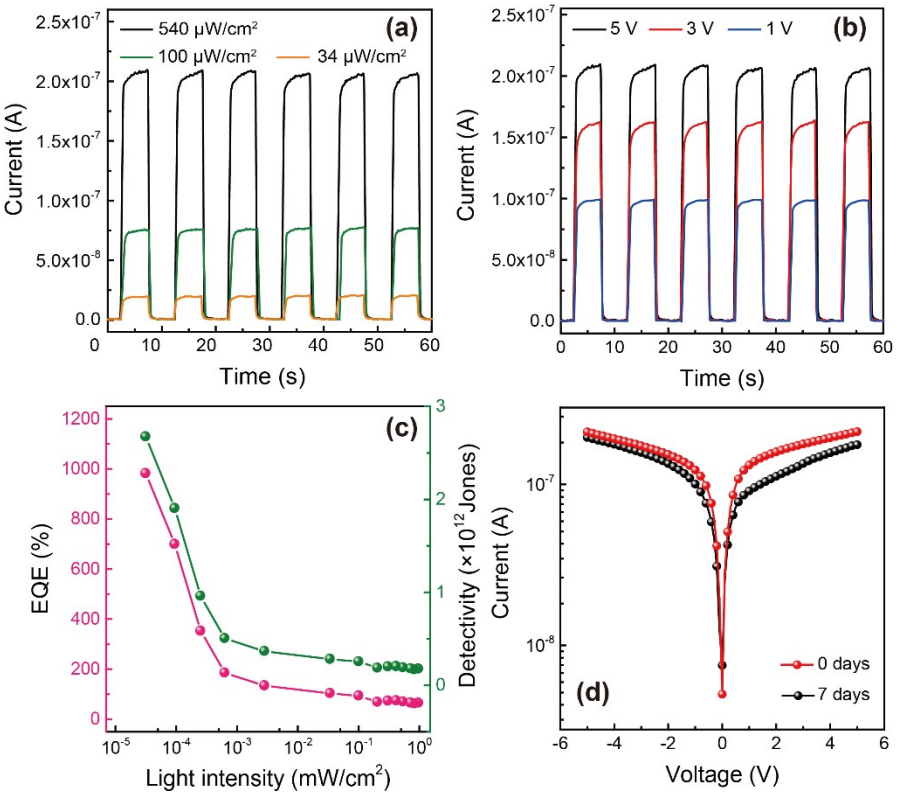

Figure S10. Time-dependent photoresponse of the photodetector measured with different light intensities **a)** and bias voltages **b)** by periodically turning on and off a 420 nm monochromatic LED light. **c)** EQE and detectivity as a function of incident light intensity under 420 nm light illumination at a bias of 5 V. **d)** The photocurrent-voltage characteristics of the photodetector and the same device stored for one week under 420 nm light illumination with the same light intensity of 540 μW cm^{-2} under 5 V bias, which demonstrate the good device stability.